Gas Hydrates in Permafrost: Distinctive Effect of Gas Hydrates and Ice on the Geomechanical Properties of Simulated Hydrate-Bearing Permafrost Sediments

J. Yang[1*], A. Hassanpouryouzband[1], B. Tohidi[1], E. Chuvilin[2], B. Bukhanov[2], V. Istomin[2], A. Cheremisin[2]

[1]Institute of Petroleum Engineering, School of Energy, Geoscience, Infrastructure and Society, Heriot-Watt University, Edinburgh, United Kingdom

[2]Skolkovo Institute of Science and Technology, Moscow, Russia

* Corresponding author: Jinhai Yang (petjy@hw.ac.uk)

Keywords: Gas hydrate; ice; triaxial shearing; sediments; geomechanical properties; micro hydrate networks

Key Points:

- Geomechanical properties of unfrozen and frozen, hydrate-free and hydrate-bearing sediments were experimentally determined.
- Ice and hydrate distinctively affected the shearing characteristics and deformation behavior of sediments.
- A physical model of micro hydrate networks was presumed as a complement to the existing hydrate models to interpret the distinctive characteristics.

Abstract

The geomechanical stability of the permafrost formations containing gas hydrates in the Arctic is extremely vulnerable to global warming and the drilling of wells for oil and gas exploration purposes. In this work the effect of gas hydrate and ice on the geomechanical properties of sediments were compared by triaxial compression tests for typical sediment conditions: unfrozen hydrate-free sediments at 0.3 °C, hydrate-free sediments frozen at -10 °C, unfrozen sediments containing about 22 vol% methane hydrate at 0.3 °C, and hydrate-bearing sediments frozen at -10 °C. The effect of hydrate saturation on the geomechanical properties of simulated permafrost sediments was also investigated at predefined temperatures and confining pressures. Results show that ice and gas hydrates distinctively influence the shearing characteristics and deformation behavior. The presence of around 22 vol% methane hydrate in the unfrozen sediments led to a shear strength as strong as those of the frozen hydrate-free specimens with 85 vol% of ice in the pores. The frozen hydrate-free sediments experienced brittle-like failure, whilst the hydrate-bearing sediments showed large dilatation without rapid failure. Hydrate formation in the sediments resulted in a measurable reduction in the internal friction, whilst freezing did not. In contrast to ice, gas hydrate plays a dominant role in reinforcement of the simulated permafrost sediments. Finally, a new physical model was developed, based on formation of hydrate networks or frame structures to interpret the observed strengthening in the shear strength and the ductile deformation.

1 Introduction

Very large volumes of methane hydrate have been found in permafrost regions in the Arctic, for example in the West Siberian basin (Cherskiy et al., 1985; Yakushev and Chuvilin, 2000; Safronov, et al., 2010), the Mackenzie Delta of Canadian Arctic (Judge and Majorowicz, 1992; Collett, 1992), and the Northern Alaska (Bird and Magoon, 1987; Collett, 1997). It is estimated that about 5×10^2 to 1.2×10^6 Tcf of methane hydrates are buried in the permafrost regions in the Arctic (Max and Lowrie, 1996). Burning methane gas produced from methane hydrate releases up to 5 times less carbon dioxide compared to burning coal (Metz el at., 2005). Therefore, gas hydrate is considered to be a potential low-carbon energy resource for the near future (Kvenvolden, 1988; Milkov, 2004; Collett, 1992; Holder et al., 1984; Max and Johnson, 2016).

Gas hydrate is a type of ice-like crystalline solid with physical properties similar to those of ice. Gas hydrate can decompose and release the gas molecules bonded in the hydrate lattice if either the temperature or pressure is outside the hydrate stability zone (HSZ) (Sloan and Koh, 2007). Based on this principle, several methods have been developed to produce methane or natural gas from gas hydrate deposits, such as depressurisation, thermal stimulation, inhibitor injection (Holder et al., 1984), and carbon dioxide (CO_2) replacement (Ohgaki, et al., 1996). In practice, the CO_2 replacement method recovers methane using CO_2-CH_4 (methane) molecule exchange by injection of CO_2-N_2 (nitrogen) mixtures or flue gas into gas hydrate deposits (Masuda et al., 2011; Schoderbek et al., 2012; Yang et al., 2017; Hassanpouryouzband et al., 2018). Drilling through permafrost layers could cause wellbore instability (Collett and Dallimore, 2002). Gas hydrates in permafrost are extremely sensitive to thermal influences due to global warming, seasonal change, geothermal fluxes, and human activities. Rising temperatures could result in hydrate decomposition hence changes in the mechanical and thermal properties of frozen hydrate-bearing sediments, creating serious geologic hazards that are responsible for methane gas blowout (Westbrook et al., 2009; Shakhova et al., 2010), sliding of seafloor and permafrost-under-laid continental slopes (Nisbet and Piper, 1998; Paull et al., 1991).

In past decades, extensive experimental investigations have been carried out to investigate how gas hydrates influence the geomechanical strength of sediments hence the slope stability of both onshore and offshore permafrost. Winter at al. (1999) determined the mechanical strength and geophysical properties of gas hydrate-bearing sediment samples that were taken from the JAPEX/JNOC/GSC Mallik 2L-38 gas hydrate research well using a purpose-built gas hydrate and sediment test laboratory instrument. For simplicity, some workers examined the mechanical properties of sediments containing tetrahydrofuran (THF) hydrate instead of methane or natural gas hydrates (Parameswaran et al., 1989; Yun et al., 2007; Lee et al., 2008). Experimental results generated using triaxial testing systems as well as direct shear apparatuses showed the mechanical properties and deformation behavior of gas hydrate-bearing sediments (Masui et al., 2005; Miyazaki et al., 2011; Hyodo et al., 2013; Yoneda et al., 2015; Santamarina et al., 2015; Liu et al., 2018). Small-strain mechanical properties of hydrate-bearing sediments such as sand, silt, and clay were investigated using resonant column apparatus (Priest et al., 2005) and bender-element devices (Lee et al., 2010). In general, the studies showed that the presence of hydrates leads to higher stiffness, shear strength and smaller pre-failure dilation. Three physical contact models proposed by Dvorkin et al. (2000) have been widely applied to describe the effect of hydrates, including pore filling, load bearing, and cementation. Moreover, apart from the mineralogical composition of sediments, initial distribution of water in pores, for example, dissolved water, partially-saturated water or water from melting ice grains is known to be one of the key factors altering gas hydrate behavior in sediments (Waite et al., 2004; Yun et al., 2007; Waite et al., 2009).

In permafrost both ice and gas hydrates may exist together. The crystal structure of ice (i.e., Ih) and clathrate gas hydrate consists of water molecules that are hydrogen-bonded in solid lattices. Water is frozen to form ice by rearrangement of water molecules into hexagonal structures at subzero temperature, whilst at low temperature and elevated pressure conditions water molecules form a network of cage-like structures (clathrate lattices) by enclosing suitably sized ‘guest’ molecules such as methane, ethane, propane and CO_2. Hydrate particles can float in pore water, bear load between sediment grains or cement sediment grains, in comparison, ice crystals always tend to stick to sediment grains. The coexistence of ice and gas hydrate plays a substantial role in the geological structure hence stabilization of both onshore and offshore permafrost. Although the mechanical and rheological properties of frozen soils have been thoroughly investigated (Vyalov, 1965; Andersland and Akili, 1967; Tsytovich, 1975; Yershov, 1998; Arenson, 2007), little work on gas hydrate-bearing frozen sediments has been reported in literature, therefore, there is lack of fundamental knowledge of unique characteristics of the ice-hydrate-bearing sediments compared to solely frozen soils or hydrate-bearing unfrozen sediments.

In recent years, mechanical properties have been investigated using a triaxial system for synthetic sediments containing both ice and hydrates of carbon dioxide or methane hydrate, and in simulated hydrate decomposition scenarios (Liu et al., 2013; Song et al., 2016). Li et al. (2016) investigated the mechanical behaviors of so-called permafrost-associated methane hydrate-bearing sediments under different recovering techniques. All these triaxial tests used mixtures of hydrate particles, ice powders, and clay (kaolinite) grains. As a result, their specimens were compacted packs of the three solid particles, lacking cohesion and cementation of ice and hydrate to the sediment grains, leading to the determined deviatoric stress and shear strength being significantly lower than other measurements (Waite et al., 2009). In this work, a new experimental method was developed to synthesize gas hydrate-bearing frozen sediments. Following the established experimental procedures, the effect of gas hydrate and ice on the geomechanical properties of simulated permafrost sediments was compared, by triaxial compression tests on frozen and unfrozen sediments in the absence and presence of methane hydrate using a purpose-built triaxial testing system. The aim was to gain a better understanding of how water freezing and hydrate bearing differently influence the geomechanical properties of hydrate-bearing permafrost.

2 Method

Triaxial shearing was carried out to determine the shearing strength and deformation behavior of artificial sediments at different conditions: at 0.3 °C (unfrozen hydrate-free), at -10 °C (frozen hydrate-free), at 0.3 °C with about 25 vol% methane hydrate (unfrozen hydrate-bearing), and at -10 °C with about 25 vol% methane hydrate (frozen hydrate-bearing). At each condition three similar specimens were sheared under three different effective confining pressures, respectively, i.e., 0.5, 1.0, and 1.5 MPa in order to determine cohesion and internal friction angle. During loading the pore pressure was maintained at 5.0 MPa to simulate permeable geological formations under a lithostatic pressure of about several hundred meters underneath ground or seafloor where permafrost is present.

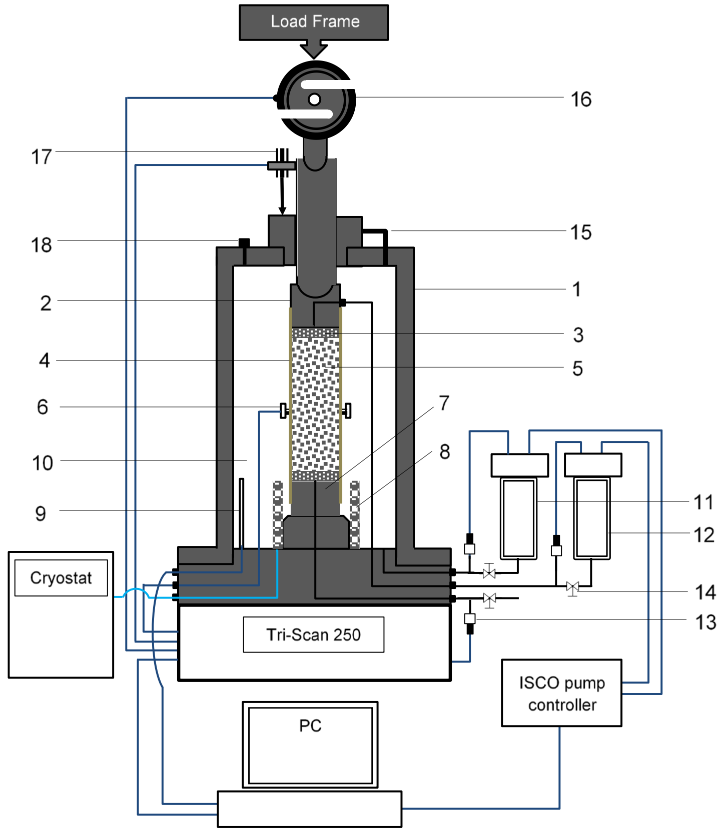

Figure 1 Schematic of the Tri-Scan 250 triaxial testing system

1-cell body, 2-top cap, 3-porous disk, 4-rubber membrane, 5-specimen, 6-radial displacement transducer, 7- base pedestal, 8-cooling coil, 9-PRT probe, 10-confining fluid, 11-ISCO pump-A (cell pressure controller), 12-ISCO pump-B (back pressure or pore pressure controller), 13-pore pressure transducer, 14-volve, 15-blanced ram assembly, 16-load cell, 17-axial LVDT, 18-air bleed bolt

2.1 Triaxial testing system

A triaxial testing system (Tri-Scan 250 from VJ Tech Ltd) was used in this work. It can work at temperatures from -20 to 50 °C and pressures up to 40 MPa to simulate the geological and thermodynamic conditions in sediments containing gas hydrates. The triaxial system consists of a high-pressure cell, a load frame (250 kN), a dual-ISCO pump pressure controller (D260), both axial and radial displacement transducers (not installed in this work), a multi-channel data acquisition module. Triaxial tests are controlled by a commercial testing software (Clisp Studio). A cooling coil is installed around the base pedestal and is connected to a cryostat (Julabo FP50) to achieve the required temperature. The system temperature is measured by a platinum resistance temperature (PRT) probe that is mounted beside the test specimen. The pore water pressure (PWP) is measured by a VJ Tech pressure transducer and the back pressure (BP) and confining pressure are measured individually by the dual ISCO pump pressure transducers. The load and axial shearing rate are measured by a load cell of the Tri-Scan 250 and a linear variable differential transmitter (LVDT), respectively. A built-in balanced ram is used to compensate the cell pressure on the ram. Figure 1 is a schematic diagram of the triaxial testing system.

2.2 Specimens

Synthetic sediments composed of 75 wt% silica sand, 20 wt% silt and 5 wt% bentonite clay were used to simulate typical loamy sand in permafrost. The silica sand was from Fife, Scotland and the silt was made by grinding the silica sand. The grain density of the sand was 2.64 g/cm^3. The bentonite clay was originally from Jembel, Turkmenistan and its grain density was 2.7 g/cm^3. Table 1 shows the mineralogical composition of the sand and clay. Figure 2 shows the particle size distribution of the sand, silt, clay and the synthetic sediment. A Malvern laser diffraction particle size analyzer (MS1000) was used to analyse the particle size of the sand and silt, while the particle size of the bentonite clay was determined by analysis of ESEM (environmental scanning electron microscope, PHILIPS XL30) images of the dry bentonite clay. The mean size and specific area are 257 μm and 0.059 m^2/cm^3 for the sand, 8.9 μm and 2.3 m^2/cm^3 for the silt, 34.6 μm and 0.71 m^2/cm^3 for the clay, respectively. The microtextures of the sediment grains were visually examined using the same ESEM. Figure 3 shows the ESEM images of the sand, silt, clay and the sediment of 75% sand + 20% silt + 5% bentonite. The sand grains are round granular particles and some of them have micro fractures, the silt grains become angular fine particles, the clay grains consist of loose and micro "plate-shaped" particles. The sediment is a mixture of the sand, silt and clay, showing complex characteristics under the ESEM. The test specimens were made of the synthetic sediment partially saturated with a water content of around 15.5 wt% to dry sediments and manually compacted in a rubber membrane sleeve of about 50 mm in diameter and 100 mm in length. Manual compaction resulted in a porosity of around 32%.

Table 1 Mineralogical composition of the silica sand/silt and clay

Silica sand	Component	Quartz	Microcline	Calcite	Kaolinite
	Ratio (wt%)	97	3	trace	trace
Bentonite clay	Component	Montmorillonite	Andesine	Biotite	Calcite
	Ratio (wt%)	93.4	2.9	2.9	0.8

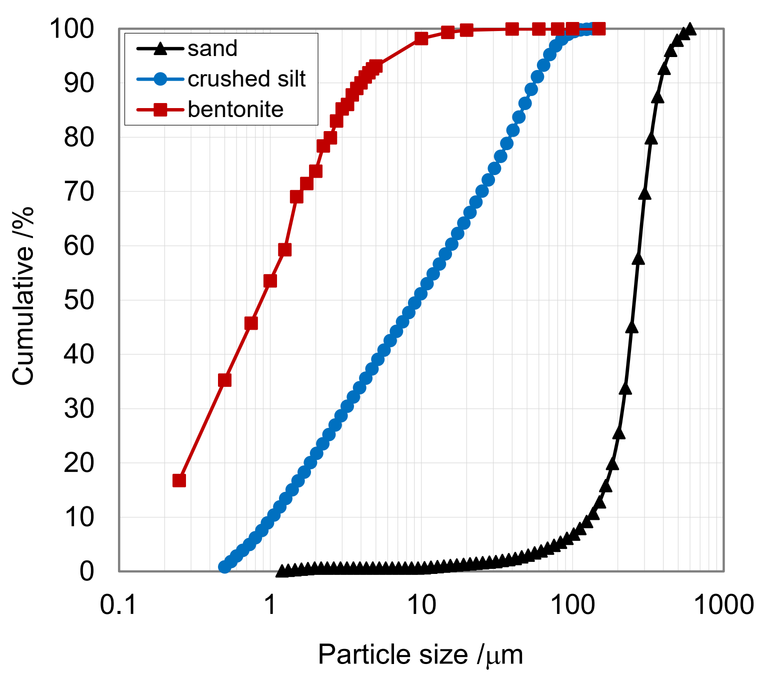

Figure 2 Particle size distribution of the silica sand, artificial silt, and bentonite clay

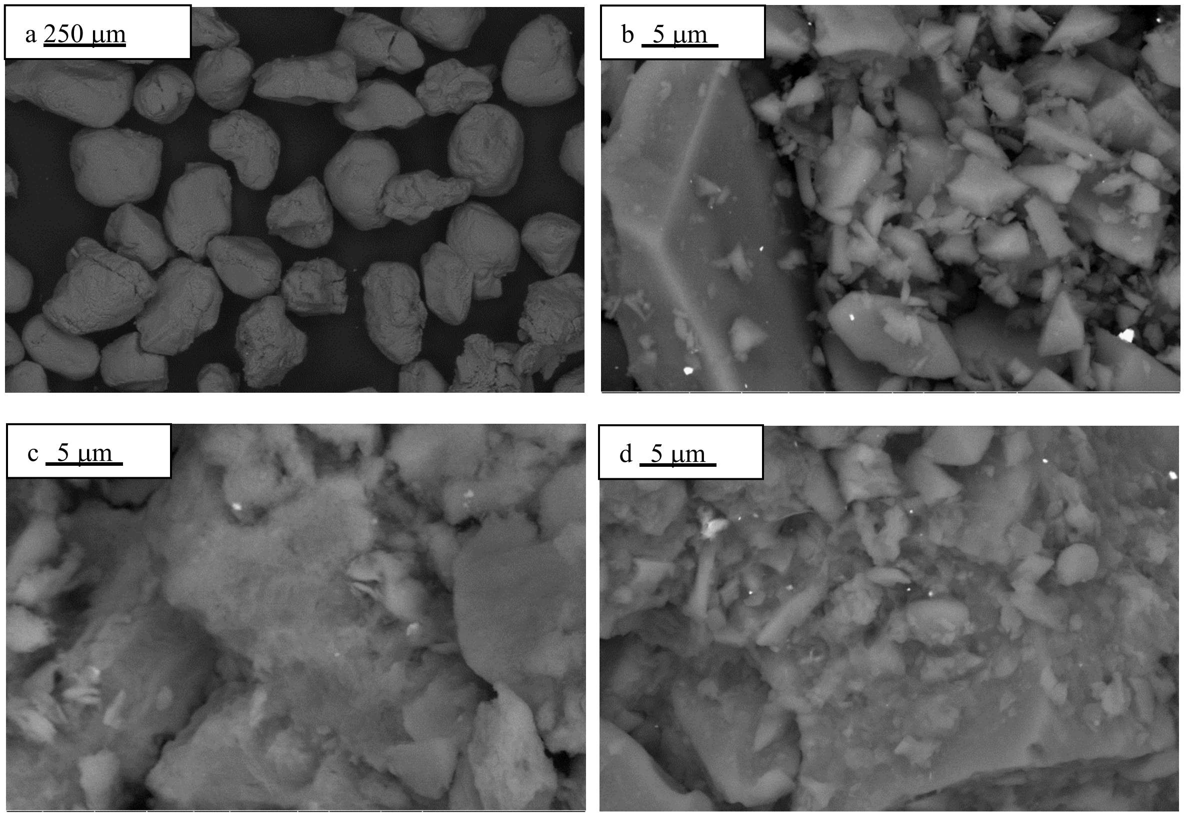

Figures 3 ESEM images of the sediment grains: (a) sand; (b) silt; (c) bentonite clay; (d) synthetic sediment.

2.3 Procedures

A wet specimen was installed and vacuum was applied to remove air present in the pores of the specimen. An effective confining pressure of 0.5 MPa was applied by injecting aqueous monoethylene glycol (MEG) solution using an ISCO pump (Pump-A in Figure 1). Then the specimen was consolidated under a load of 0.5 MPa for 1 to 2 hours until the axial creep strain rate of the specimen became smaller than 5.6×10^{-8} 1/S (i.e., axial creep less than 0.01 mm in half an hour). Methane was injected into the pre-consolidated specimen until the pore pressure reached 15 MPa at room temperature, while the confining pressure was increased simultaneously to maintain a constant effective confining pressure of around 0.5 MPa. The methane-pressurised specimen was directly cooled down to a target temperature just above 0 °C to form hydrate. During cooling and hydrate formation, the confining pressure was adjusted to maintain the confining pressure around 0.5 MPa above the pore pressure. After completion of hydrate formation which was indicated by a constant pore pressure, the effective confining pressure was adjusted to the desired value, for example, 0.5, or 1.0, or 1.5 MPa, and the cell temperature was set to the shearing temperature, 0.3 °C for unfrozen specimens and -10 °C for frozen specimens. After freezing, the pore pressure was gradually reduced to, and maintained at 5 MPa by connecting to a piston vessel in which the pressure was controlled by another ISCO pump (Pump-B in Figure 1). The system was left at the desired temperature, pore pressure, and confining pressure over night to allow the system to settle at the shearing conditions.

The porosity (ϕ) of the specimen was determined based on the known grain density of sediments and the dimensions of specimens:

$$\phi = 1 - \frac{M}{V_t \rho_s} \qquad (1)$$

where M is the mass of the dry specimen, ρ_s is the average grain density of the sediment (i.e., a sum of the product of the weight ratio and the density of each mineral component), $V_t = \pi R^2 H$ is the bulk volume of the specimen, where R and H are the radius and height of the specimen, respectively. Methane hydrate saturation (S_h) was calculated using Equation 2:

$$S_h = \frac{V_h}{V_p} = ((\frac{M_{CH4}}{M_g} - \frac{PV}{ZRT})(M_g + M_w\gamma))/(V_p\rho_h) \quad (2)$$

where V_h and V_p are the methane hydrate volume and pore volume, respectively. M_g and M_w are the molecular weight of methane and water, respectively. M_{CH4} is the mass of the injected methane. P, T, and V represent the pore pressure, temperature, and gas volume. Z is the compressibility factor of methane gas and R is gas constant. γ is hydration number and ρ_h is the bulk density of gas hydrate. For methane hydrate, $M_g = 16$, $M_w = 18$, $\gamma \cong 6.0$, $\rho_h \cong 0.92$ g/cm^3. After hydrate formation the water saturation (S_w) and gas saturation (S_g) were calculated:

$$S_w = \frac{V_w}{V_p} = (V_{w0} - (\frac{M_{CH4}}{M_g} - \frac{PV}{ZRT})\frac{\gamma M_w}{\rho_w})/V_p \quad (3)$$

And

$$S_g = \frac{V_g}{V_p} = 1 - S_h - S_w \quad (4)$$

where V_w and V_{w0} represent the water volume after and before hydrate formation, respectively; ρ_w is the density of water, i.e., 1 g/cm^3. In this work it was assumed water was completely frozen at -10 °C, therefore, ice saturation was calculated using the water saturation divided by the ice density (approximately 0.92 g/cm^3).

3 Results and Discussion

It has been reported that frozen hydrate-bearing sediments appear to have a much lower permeability compared to unfrozen ones in the absence of gas hydrate (Seyfried and Murdock, 1997; Konno et al., 2015). Consequently, the shearing rate was set at 0.1%/min mainly to prevent any excess pressure in the pores during compression, giving enough time to allow pore pressure changes to equalise throughout the specimen (Head, 1998). Furthermore, a strain rate of 0.1%/min was commonly applied to shear sediment specimens containing gas hydrates by other workers (Miyazaki et al., 2011; Hyodo et al., 2013; Liu et al., 2013; Li et al., 2016). Table 2 shows the initial parameters of the specimens before shearing. It should be noted that the unfrozen water content at -10 °C was estimated less than 3% in the specimens based on Istomin et al. (2017), therefore, this was neglected in the calculated ice saturation in Table 2.

Table 2 Initial physical parameters of specimens before shearing

Initial specimen parameters	Tests		
Unfrozen and hydrate-free	Test 1-0.5	Test 1-1.0	Test 1-1.5
Water ratio (wt%) (vol%)	15.2 (81.2)	15.3 (85.5)	15.3 (90.2)
Hydrate saturation (vol%)	0.0	0.0	0.0
Gas saturation (vol%)	18.8 (N_2)	14.5 (N_2)	9.8 (N_2)
Water saturation (vol%)	81.2	85.5	90.2
Frozen and hydrate-free	Test 2-0.5	Test 2-1.0	Test 2-1.5
Water ratio (wt%) (vol%)	15.5 (86.7)	15.5 (84.9)	15.5 (83.0)
Hydrate saturation (vol%)	0.0	0.0	0.0
Gas saturation (vol%)	13.3 (N_2)	15.1 (N_2)	17.0 (N_2)
Ice saturation (vol%)	86.7	84.9	83.0
Unfrozen and hydrate-bearing	Test 3-0.5	Test 3-1.0	Test 3-1.5
Water ratio (wt%) (vol%)	15.5 (86.3)	15.5 (86.4)	15.5 (86.7)
Hydrate saturation (vol%)	25.5	24.3	27.9
Gas saturation (vol%)	8.6	8.8	7.7
Water saturation (vol%)	65.9	66.9	64.4

Frozen and hydrate-bearing	Test 4-0.5	Test 4-1.0	Test 4-1.5
Water ratio (wt%) (vol%)	15.6 (85.4)	15.5 (85.2)	15.5 (86.8)
Hydrate saturation (vol%)	21.1	22.4	23.6
Gas saturation (vol%)	10.4	10.4	8.5
Ice saturation (vol%)	68.5	67.2	67.9

3.1 Shear characteristics

Unfrozen hydrate-free Figure 4 shows the logged evolution of the deviator stress with the axial strain. In Test 1 at 0.3 °C in the absence of methane hydrate, the unfrozen hydrate-free specimen behaved like typical soils under 0.5 MPa of effective confining pressure. When loading started, the deviator stress almost vertically increased to 0.7, 0.5, 0.7 MPa under a confining pressure of 0.5, 1.0, and 1.5 MPa, respectively, and then the sand-silt-bentonite clay grains were compacted so that the deviator stress gradually increased. Similar stress-strain behavior was also observed by other workers (Azhar et al., 1026; Della et al., 2016). The maximum deviator stress resulted in a collapse of the compacted sediment grains, leading to relatively open structure like micro fractures and the grains were forced to move downward into the void spaces. The grain compaction and downward movement were relatively slow processes, which is corresponding to the slow and long strain softening process after the peak strength was reached. Under the higher effective confining pressure of 1.0 and 1.5 MPa, the specimens were further compacted thus appearing as dense soils. By comparison with the specimen under 0.5 MPa of confining pressure, the deviator stress increased relatively steeply and fell off once the maximum deviator stress was reached, which could be attributed to the fact that the sediment grains along the shearing plane rode over each other. It should be noted that two events happened to the specimen under 1.0 MPa of confining pressure (the blue round points in Test 1). The discontinuity just before the peak stress in the deviator stress-axial strain curve was due to a brief pause of the shearing process to solve a mechanical problem. Next, the sharp drop in the deviator stress resulted from breakage of the rubber membrane.

Frozen hydrate-free For the hydrate-free specimens frozen at -10 °C (Test 2), the initial cohesiveness increased to 2.0 MPa for the three effective confining pressures. The deviator stress vertically rose to about 2.0 MPa at the beginning of shearing. This suggests that the ice cemented the sediment grains against the initially applied loading. Gradual strain hardening started following that, which is similar to that observed in the unfrozen hydrate-free sediments in Test 1. By contrast with the unfrozen specimens at 0.5 °C, sharp strain softening occurred once the failure point was reached. At the end of shearing (at an axial strain of 13.5%, 26.0%, and 28.2% under 0.5, 1.0, and 1.5 MPa, respectively), somewhat brittle characteristic of the specimens frozen at -10 °C was observed. As shown in Table 2, ice filled about 85% of the pore volume after freezing. We interpret the brittle-like failure resulting from the breakage of crystalline ice structures in the specimens.

Unfrozen hydrate-bearing In Test 3 with the unfrozen specimens containing about 22 vol% of methane hydrate at 0.3 °C, the gradual compression started at about 1 MPa, a little higher than those of the unfrozen hydrate-free specimens in Test 1 and half of the frozen hydrate-free specimens in Test 2. The deviator stress steeply rose to higher than 1 MPa during the initial compression, which was similar to that observed in the hydrate-free specimens frozen at -10 °C. This could be evidence that methane hydrate did cement the sediment grains to some extent. Then the deviator stress linearly increased as the axial strain increased. After the deviator stress reached a peak, strain softening started. No brittle failure points appeared. These characteristics are in contrast to those observed for the unfrozen hydrate-free sediments at 0.3 °C and the frozen hydrate-free sediments at -10 °C. The result may suggest that the presence of about 22% methane hydrate not only strengthened the sediment but also made the unfrozen sediment more ductile compared to the brittle-like failure of the frozen sediments in the absence of methane hydrate. After the peak stress the deviator stress fluctuated in a small range, which could be an indication that hydrate crystals became detached from the sediment grains or resisted grains riding over each other (Yun et al., 2007). It should be noted that the difference in the gas saturation (Table 2) might also be a factor contributing to the strengthening effect observed in Test 2 (freezing) and Test 3 (hydrate bearing), although the ice saturation in Test 2 is much higher than that of methane hydrate in Test 3.

Frozen and hydrate-bearing In comparison with the Tests 1-3, the specimens with methane hydrate of 21.1 to 23.6% and frozen at -10 °C showed that the gradual compression did not start until the deviator stress reached 2 MPa, which is similar to those measured in Test 2. This suggests that ice enhanced cohesiveness more than these saturations of methane hydrate did. Apart from the highest peak shear stress, brittle-like failure occurred in the frozen hydrate-bearing specimens. Given that brittle-like failure was also observed for the frozen hydrate-free specimens in Test 2, the presence of a low saturation of methane hydrate did not alter the brittle-like failure of the frozen specimens (Arenson et al. 2007). Furthermore, the stress-strain curves of the frozen hydrate-bearing sediments look smoother than the others. This could be related to the fact that the specimens had the lowest void after methane hydrate formation and freezing. This indicates that the high porosity filling of ice and hydrate led to smaller void spaces for the sediment grains to move downwards during compression.

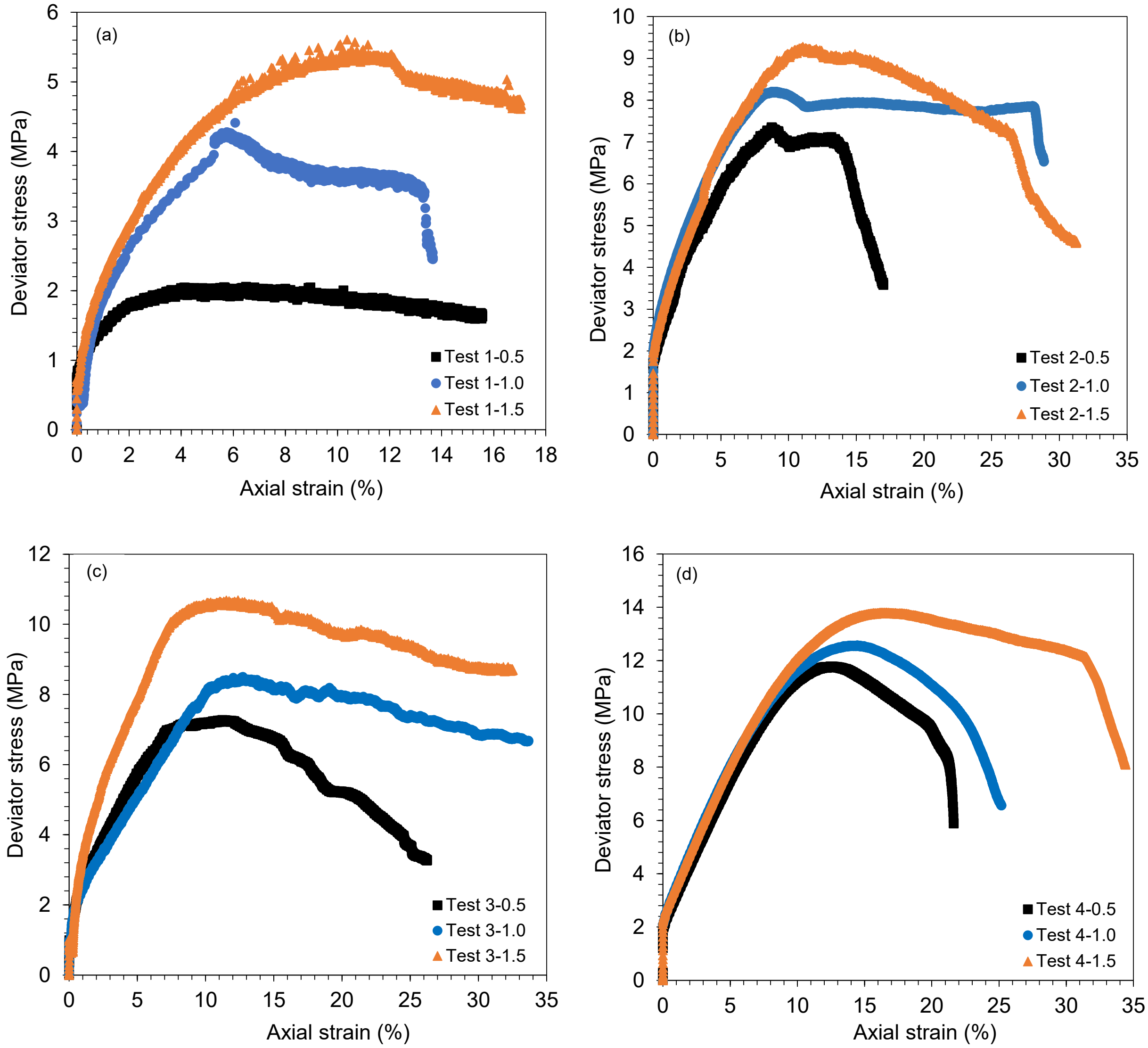

Figure 4 Shear characteristics of unfrozen and frozen sediments in the absence and presence of methane hydrate. (a) Test 1: hydrate-free at 0.3 °C, (b) Test 2: hydrate-free and frozen at -10 °C, (c) Test 3 with methane hydrate at 0.3 °C, and (d) Test 4 with methane hydrate frozen at -10 °C. In the legend the numbers “0.5, 1.0, 1.5” denote the effective confining pressures in MPa.

3.2 Deformation behavior

Volume strain was measured to reflect the deformation behavior of the sediments during shearing. The ISCO Pump-B was connected to a piston vessel that was full of methane (not shown in Figure 1). The outlet of the methane gas vessel was connected to the PWP port and the backpressure port of the triaxial cell. Changes in the specimen pore volume can be measured by the ISCO Pump-B set at the desired pore pressure. Given that the sediment grains are incompressible under the experimental pressure, the changes in the bulk volume of a specimen should be equal to the changes in the pore volume of the specimen. Expansion of a specimen in volume is called dilation, corresponding to a negative volume strain and compression in volume means a positive volume strain. Figure 5 illustrates the determined cumulative volume strain versus axial strain.

Unfrozen hydrate-free In Test 1, under 0.5 MPa of confining pressure, the initial volume strain of zero indicates the unfrozen hydrate-free specimen experienced a little lateral expansion, which was balanced by the axial compression at a rate of 0.1 mm/min. Then continuous dilatation occurred while axial compression proceeded. Given that the pore pressure was maintained at 5 MPa, it could be expected that fine fractures or voids were formed due to the sediment grains riding over each other, leading to lateral expansion. When the confining pressure was at 1.0 MPa, the measured volumetric strain was zero until the membrane was broken at 13.5% of axial strain. (The membrane breakage led to a vertical rise of the volumetric strain-axial strain curve). This suggests that the specimen had been experiencing a literal dilatation that was consistently equal to the axial compression. Under 1.5 MPa of confining pressure, the specimen showed larger compression and then the specimen volume remained constant after a quick compression at about 2% of axial strain, i.e., it laterally dilated at a rate at which it was axially compressed. Quick dilatation occurred at about 12% of axial strain where the peak deviator stress was reached (Figure 4). The higher the confining pressure, the smaller the dilatation, because the confining stress tends to hold the sediment grains together by increasing the inter-particle forces such as internal friction force and interlock force against the lateral expansion.

Frozen hydrate-free For the hydrate-free sediments, freezing at -10 °C significantly reduced the dilatation of the specimens during shearing. This is attributed to the fact that ice crystals cemented the sediment grains and filled more void spaces than the original water did. The specimens quickly collapsed once the failure stress was reached, which is indicated by the sharp falling of the volumetric strain-axial strain curves.

Unfrozen hydrate-bearing At 0.3 °C, the specimens whose void spaces were filled with about 22 vol% methane hydrate slightly dilated in radial direction while compressed in its length. Continuous large dilatation did not start until the failure deviator stress was reached. After the failure points, large dilatation gradually occurred and no sudden dilatation was observed throughout shearing. By comparison with the unfrozen hydrate-free sediments in Test 1 and the frozen hydrate-free sediments in Test 2, it could be said that the presence of about 22 vol% methane hydrate enhanced the shear strength as much as the sediments frozen at -10 °C and made the unfrozen hydrate-bearing sediments less brittle than those hydrate-free sediments frozen at -10 °C. However, the low saturation of methane hydrate could not hinder lateral expansion as freezing at -10 °C did. Increase in confining pressure led to significant reduction in dilatation.

Frozen hydrate-bearing In Test 4 the specimens were formed with an average saturation of about 22 vol% and frozen at -10 °C. The presence of both methane hydrate and ice further limited lateral expansion and delayed the occurrence of quick dilatation compared to the frozen and hydrate-free specimens in Test 2 and the unfrozen hydrate-bearing specimens in Test 3.

Similar characteristics of volumetric strain were observed for frozen soils by Zhang et al. (2007). However, some particulars of the observed deformation behavior are different from other frozen soils (Arenson and Springman, 2005). This could be attributed to the fact that there is no literature reporting triaxial compression experiments that are really comparable with this work: specific synthetic loamy sand sediments sheared at constant pore pressure and in the presence of water, gas, ice, and methane hydrate in pores.

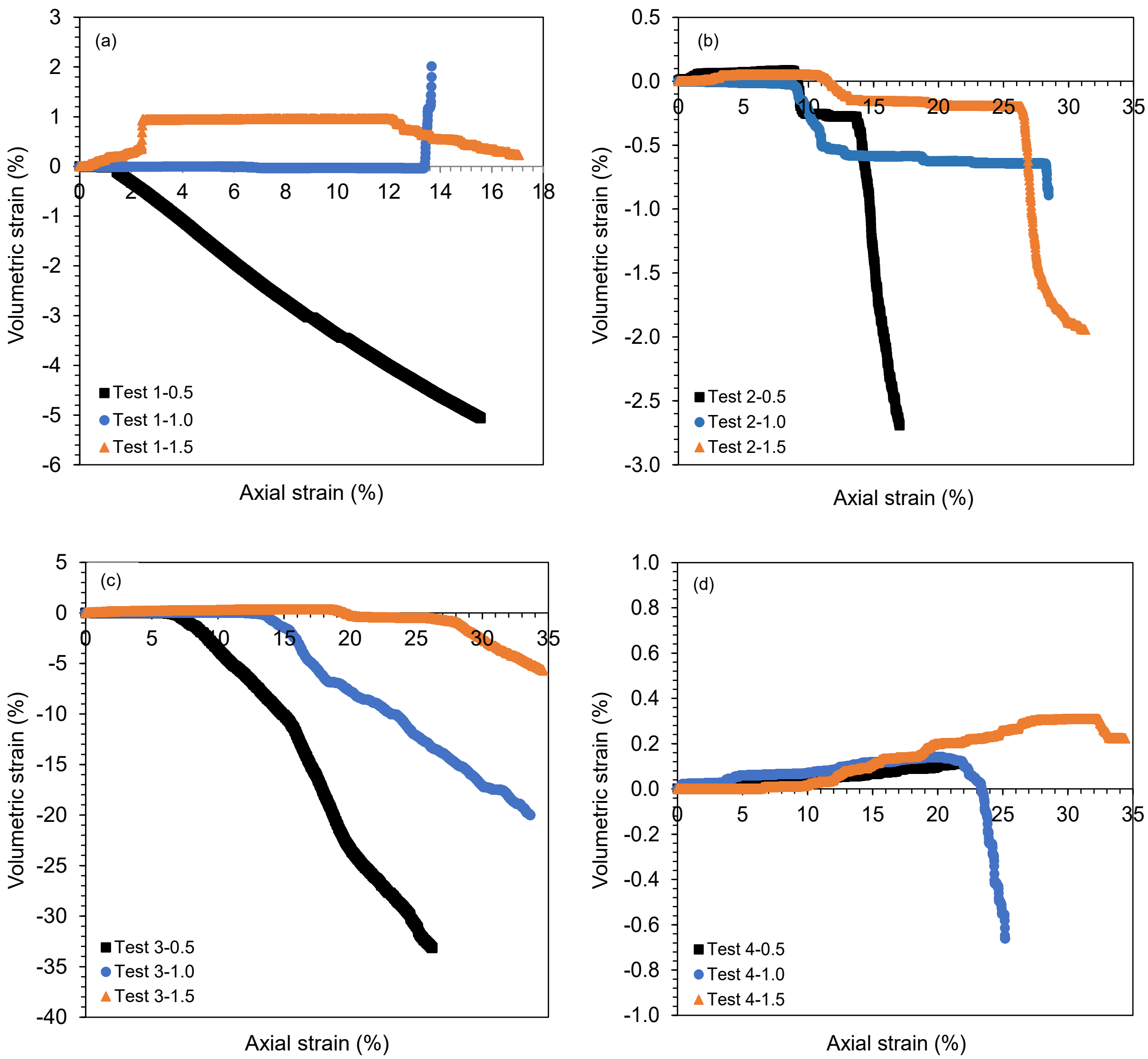

Figure 5 Deformation behavior of unfrozen and frozen sediments in the absence and presence of methane hydrate. (a) Test 1: hydrate-free at 0.3 °C, (b) Test 2: hydrate-free and frozen at -10 °C, (c) Test 3 with methane hydrate at 0.3 °C, and (d) Test 4 with methane hydrate frozen at -10 °C.

3.3 Determined mechanical properties

Mechanical properties were determined and shown in Table 3, including shear strength τ, stiffness (scant Young's modulus E_{50}), cohesion C and angle of internal friction ϕ, (P_{ec} denotes effective confining pressure). The scant Young's modulus was determined tangentially from the start to the middle of the linear section of the stress versus strain curves in Figure 4. The cohesion and friction angle were determined according to Mohr-Coulomb equation in terms of effective stress (Das, 1997). As a typical example, Figure 6 represents the Mohr-Coulomb circles for determination of the cohesion and friction angle of the frozen hydrate-free sediments in Test 2.

Table 3 The determined shear strength, stiffness, cohesion, and friction angle

Test	P_{ec} (MPa)	τ (MPa)	E_{50} (MPa)	C (MPa)	ϕ (°)
	0.5	2.6	80		
Test 1	1.0	5.4	95	0.1	38.0
	1.5	7.0	106		
	0.5	7.9	110		
Test 2	1.0	9.2	119	1.9	39.5
	1.5	10.8	107		
	0.5	7.7	117		
Test 3	1.0	9.5	86	1.2	29.2
	1.5	12.3	201		
	0.5	12.3	112		
Test 4	1.0	13.6	122	3.0	31.5
	1.5	15.3	117		

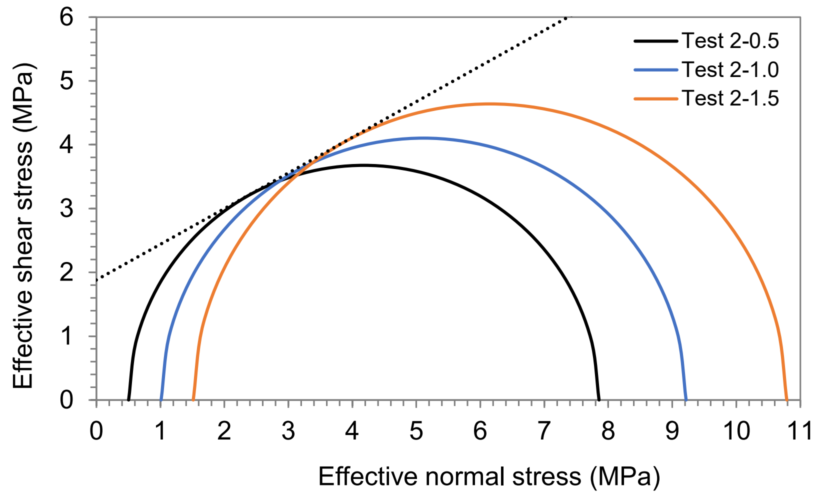

Figure 6 Mohr-Coulomb circle of Test 2 with specimens frozen at -10 °C in the absence of hydrate

Figure 7 illustrates the effect of hydrate bearing and freezing on shear strength. Under the same confining pressure, the hydrate-free sediments frozen at -10 °C (Test 2) were mechanically stronger than the unfrozen hydrate-free sediments at 0.3 °C (Test 1); the unfrozen sediments with around 22 vol% methane hydrate (Test 3) were at least as strong as the frozen hydrate-free sediments with an average ice saturation of around 85 vol%. The presence of methane hydrate in about 22 vol% of the pore spaces led to a shear strength similar to that by ice filling 85 vol% of the pore spaces. Only based on the existing mechanisms such pore filling, load bearing and grain cementation, it cannot be fully understood why such a low saturation of methane hydrate resulted in a mechanical strength similar to freezing at -10 °C, even if hydrate crystals tend to cement the sediment grains in partially water-saturated sediments (Waite et al., 2004). In Test 4 the specimens which were formed with about 22 vol% methane hydrate and frozen at -10 °C show the highest shear strength compared to the other three groups of specimens. Moreover, the presence of about 22 vol% methane hydrate led to similar enhancement of the shear strength for both unfrozen and frozen specimens. Finally, it can also be seen that the shear strength increases as the confining pressure rises.

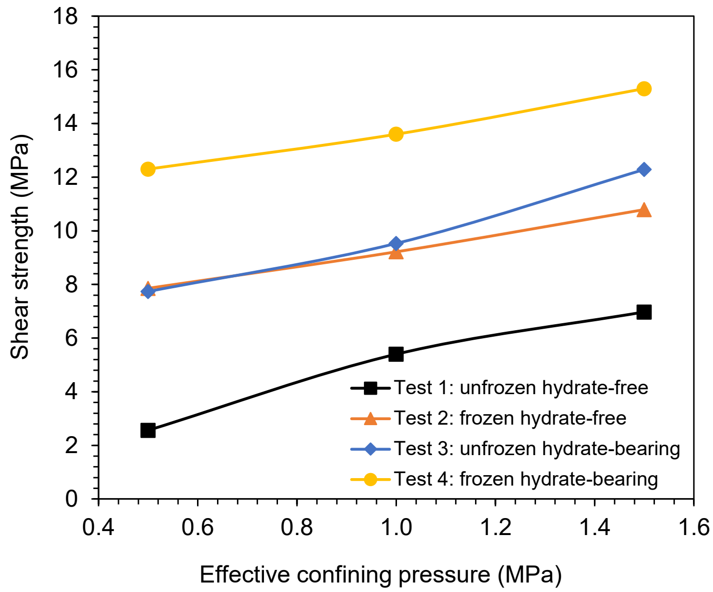

Figure 7 The determined shear strength shows the effect of hydrate bearing and freezing on shear strength.

In Table 3 the measured cohesion and angle of internal friction of the unfrozen and hydrate-free specimens in Test 1 is very small. This is because the specimens were of normally consolidated sand-silt-clay packs (Mitchell, 1993; Das, 1997). The presence of methane hydrate and freezing significantly increased the cohesion of the sediments by hydrate and ice cementing. However, it is interesting to see that hydrate formation in the specimens resulted in reduction in the internal friction, whilst freezing did not. This means that the presence of 22 vol% of methane hydrate appeared to be weakening the inter friction and interlocking between the grains, causing the large dilatation observed in the unfrozen hydrate-bearing sediments in Test 3 (Figure 5). To the best of our knowledge, no such experimental observations have been reported. One hypothesis could be due to particle assemblages (Mitchell, 1993). Methane hydrate crystals might locally bond together the fine clay and silt particles as well as sand particles, forming particle lumps that were wrapped with hydrate crusts. The hydrate-wrapped particle lumps behaved as loose sand particles so that the friction angle reduced to the typical range of loose sand (Das, 1997). The measured scant Young's modulus in Table 3 shows that the presence of hydrate and ice measurably increased the stiffness of the specimens. However, it seems that hydrate-bearing did not create much change in the stiffness of frozen sediments.

3.4 Effect of gas hydrate saturation

One series of triaxial experiments were conducted to investigate the effect of hydrate saturation on the geomechanical properties of simulated permafrost sediments. The same synthetic sediments were used to make the specimens. The specimens were formed with different saturations of methane hydrate and frozen at -3.0 °C. Shearing was performed at the same conditions: temperature -3.0 °C, pore pressure 5.0 MPa, effective confining pressure 1.0 MPa, and shearing rate 0.1 mm/min. Table 4 shows the saturation of methane hydrate, ice and gas before shearing.

Table 4 Saturation of methane hydrate, ice, and gas

Initial specimen	Test 5	Test 6	Test 7	Test 8	Test 9
Hydrae saturation (vol%)	0.0	16.7	27.4	33.2	51.7
Gas saturation (vol%)	12.1	9.2	9.0	15.7	17.6
Ice saturation (vol%)	87.9	74.1	63.6	51.1	30.7

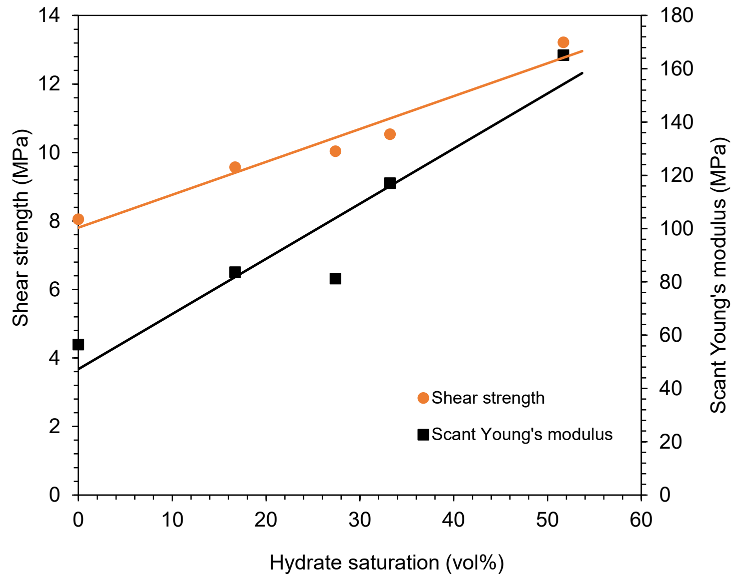

Figure 8 Effect of different saturations of methane hydrate on the shear strength and stiffness of frozen sediments

Figure 8 shows that the determined shear/peak strength and stiffness linearly increase as the hydrate saturation increases. Similar linear relationships between shear strength and stiffness versus hydrate saturation were also reported for unfrozen silica sand containing methane hydrate (Masui et al., 2005; Miyazaki et al. 2011). The determined shear strength is largely higher than those reported by Liu et al. (2013), Sone et al. (2016), and Li et al. (2016). As mentioned in the Introduction, this is because different methods were used to make the simulated permafrost sediments. It should be noted that from Specimens 5 to 9, the shear strength gradually increased with the increase in methane hydrate saturation even if the ice saturation in the specimens decreased. This result suggests that gas hydrate plays a dominant role in the geomechanical properties of the simulated permafrost sediments.

4 Physical model of hydrate reinforcement of sediments

The existing models of gas hydrate particle association, i.e., pore filling, load bearing and cementation, are insufficient to fully interpret why the presence of only around 22 vol% methane hydrate at 0.3 °C (Test 3 in Figure 4) resulted in a shear strength as strong as around 85 vol% of water frozen at -10 °C (Test 2 in Figure 4), and made the unfrozen hydrate-bearing specimens more ductile compared to those with the frozen hydrate-free ones. One of the possible explanations is that the intrinsic strength of methane hydrate is 20 to 30 times stronger than that of ice at a temperature near the freezing point (Durham, 2003). Moreover, water films between hydrate crusts or crystals and grain surfaces (Chaouachi et al., 2015; Yang et al., 2016), unfrozen water (Chamberlain et al., 1972), and pressure melting (Goodman et al., 1979; Jones et al., 1982) in the sediments further weakens the interparticle contacts by reducing the internal friction force and interlocking interaction. However, these factors fail to explain the unexpectedly high effect of a low hydrate saturation on the mechanical properties of sediments in comparison with freezing at – 10 °C.

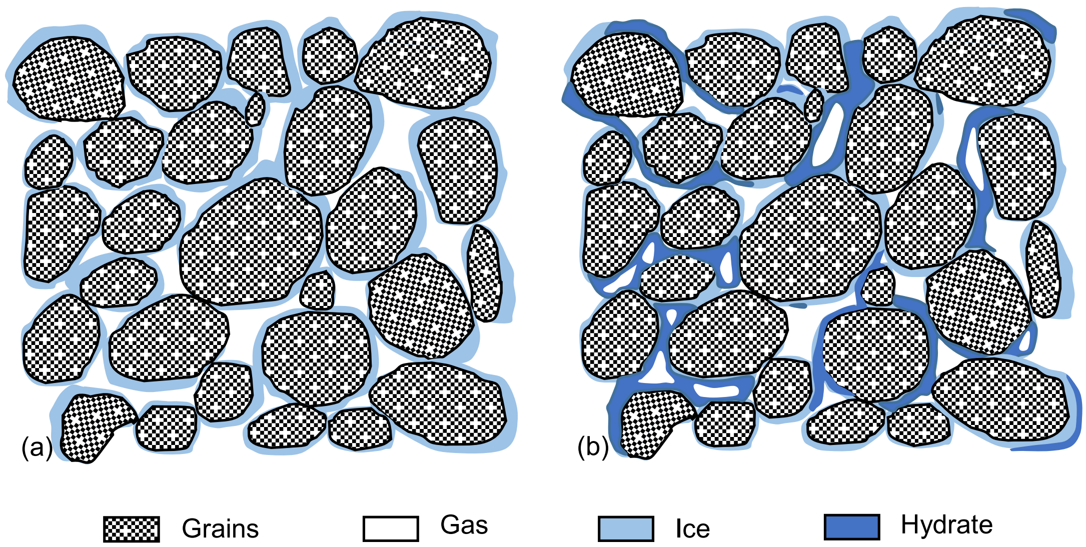

Figure 9 Schematic of the hypothetical hydrate networks or frame structures. (a) Ice wraps sediment grains with point-contact, (b) Hydrate networks extend across adjacent grains.

In partially water-saturated sediments, as shown Figure 9a, it is likely that water attached to the surface of the sediment grains in addition to some of the water absorbed by the clay (Waite et al., 2004). Ice formed from the water partially filling sediment pores cements the grains mostly at the grain-grain contacts or very limited areas adjacent to grain contact points. On the other hand, this type of water distribution makes it possible to connect the remaining pore spaces and form channels. The injected methane gas fills these channels and appears as gas bubbles that are surrounded by water. Methane hydrate always starts to form at the interface between water and methane gas, transforming the gas bubbles into either gas-filled or solid methane hydrate crystalline bars. These hydrate bars can grow locally or extend across adjacent grains through a mass transfer process and finally create mini or macro hydrate networks or hydrate frame structures throughout the specimens. In addition to the existing position models aforementioned, these hydrate-associated structures substantially enhance the shear strength of the specimens and make them significantly more ductile, just like reinforcing concrete using steel bars. Figure 9b illustrates the schematic modes of the gas hydrate networks or frame structures. As a result, it is presumed that, apart from the existing models of hydrate location in pores including pore filling, load bearing, and cementation, the patterns or morphology of hydrate crystals should be considered to understand the effect of hydrate bearing on the mechanical properties of sediments.

It is plausible to anticipate the effect of micro hydrate frame structures may substantially depend on initial water content and distribution in sediments before hydrate and ice formation. The typical water saturation of about 86.5 vol% to pore volume (15.5 wt% to dry sediments, Table 2) was used in this work, which leads to the strong effect of the micro hydrate frame structures. Observations of gas hydrate formation using synchrotron X-ray microscopy technique and magnetic resonance imaging technique suggested that gas hydrate crusts tend to form and wrap sediment grains in the presence of a very low water content, whilst it is likely that hydrates start to form at gas-water interfaces, grow into the water body and suspend in the water (Chaouachi et al., 2015; Yang et al., 2016; Zhao et al., 2014). Consequently, changes in initial water saturation may alter the structure of the micro hydrate network in permafrost sediments. More experiments have been planned to further investigate how initial water saturation affects geomechanical properties of hydrate-bearing permafrost sediments.

5 Conclusions

The shear characteristics and deformation behavior of four types of artificial sediments were investigated at different conditions, including unfrozen hydrate-free, frozen hydrate-free, unfrozen hydrate-bearing, and frozen hydrate-bearing sediments. Results show that ice and gas hydrates distinctively affect the shearing characteristics and deformation behavior of the specimens, though they are both water-based crystalline solids.

- Both methane hydrate and ice significantly enhanced the shear strength of sediments. Under the same confining pressure the presence of 25 vol% methane hydrate in the unfrozen sediments led to a shear strength as strong as those of the frozen hydrate-free specimens in which 86 vol% of the pore spaces were occupied by ice at -10 °C. Coexistence of both gas hydrate and ice resulted in the highest shear strength. Additionally, the unfrozen hydrate-bearing sediments and the frozen hydrate-free sediments showed the initial cohesiveness of about 2.0 and 1.0 MPa, respectively, compared to about 0.6 MPa of the unfrozen hydrate-free sediments.

- The sediments that were initially saturated with about 85 vol% of water frozen at -10 °C experienced brittle-like failure. In contrast, those sediments containing about 25 vol% methane hydrate showed large dilatation but no quick failure occurred.
- The presence of methane hydrate and freezing significantly increased the cohesion of the sediments by hydrate and ice cementing. However, hydrate formation in the sediments resulted in measurable reduction in the internal friction, whilst freezing did not.
- Methane hydrate plays a dominant role in the geomechanical properties of the simulated permafrost sediments.
- It was found that the existing hydrate position models seem insufficient to interpret the large strengthening in the shear strength and the ductile deformation for the low saturation of methane hydrate. As a result, it was hypothesized that formation of hydrate networks or frame structures may play a substantial role in the observed reinforcement of both unfrozen and frozen sediments.

Acknowledgement

The authors would gratefully acknowledge the financial support from the Skolkovo Institute of Science and Technology (Russia). The authorswould also thank Dr Jim Buckman for the ESEM images of the sediments, Mr Mehrdad Vasheghani Farahani for his help in analysis of particle size of the bentonite clay, and Dr Rod Burgass for his valuable comments on the manuscript. The data for this paper can be found in the supporting information.

References

Andersland D.B. and Akili W. (1967). Stress effect on creep rates of a frozen clay soil. *Geotechnique*, **17**, 27-39.

Arenson L.U. (2007). The rheology of frozen soils. *Applied Rheology*, **17** (1), 12147-1−12147-14.

Arenson L.U. and Springman S.M. (2005). Triaxial constant stress and constant strain rate tests on ice-rich permafrost samples. *Canadian Geotechnical Journal*, **42**, 412–430.

Azhar A.T.S., Norhaliza1 W., Ismail1 B., Abdullah1 M.E., Zakaria1 M.N. (2016). Comparison of shear strength properties for undisturbed and reconstituted Parit Nipah Peat, Johor. *Materials Science and Engineering,* **160**, 012058, doi:10.1088/1757-899X/160/1/012058.

Bird K.J. and Magoon L.B. (1987). Petroleum geology of the northern part of the Arctic National Wildlife Refuge, Northeastern Alaska. In: U.S. *Geological Survey Bulletin*, 1778.

Chamberlain E., Groves C., Perham R. (1972). The mechanical behaviour of frozen earth materials under high pressure triaxial test conditions. *Géotechnique*, **22** (3), 469-483.

Chaouachi M., Falenty A., Sell K., Enzmann F., Kersten M., Haberthür D., Kuhs W.F. (2015). Microstructural evolution of gas hydrates in sedimentary matrices observed with synchrotron X-ray computed tomographic microscopy. *Geochemistry, Geophysics, Geosystems*, **16**, 1711-1722.

Cherskiy N.V., Tsarev V.P., Nikitin S.P. (1985). Investigation and prediction of conditions of accumulation of gas resources in gas-hydrate pools. *Petroleum Geology*, **21**, 65-89.

Collett T.S. (1992). Potential of gas hydrates outlined. *Oil & Gas Journal*, **90**, 84-87.

Collett T.S. (1997). Gas hydrate resources of northern Alaska. *Bulletin of Canadian Petroleum Geology*, **45**, 317-338.

Collett T.S. (2005). Results at Mallik highlight progress in gas hydrate energy resource research and development. *Petrophysics*, **46** (3), 237–243.

Collett T.S., Dallimore S.R. (2002). Detailed analysis of gas hydrate induced drilling and production hazards: Proceeding of the 4th International Conference on Gas Hydrates, 47-52, Yokohama, Japan.

Das B.M. (1997). *Advanced Soil Mechanics (Second Edition)*. Taylor & Francis: Washington DC, USA. 314-322.

Della N., Muhammed R.Z., Canou J., Dupla J.C. (2016). Influence of initial conditions on liquefaction resistance of sandy soil from Chlef region in Northern Algeria. *Geotechnical and Geological Engineering,* **34**, 1971–1983.

Durham W.B. (2003). The strength and rheology of methane clathrate hydrate. *Journal of Geophysical Research*, **108**, B4, 2182.

Dvorkin W.B., Helgerud M.B., Waite W.F., Kirby S.H., Nur A. (2000). Introduction to physical properties and elasticity models. *Natural Gas Hydrates in Oceanic and Permafrost Environments*, Max M. ed, 245.

Goodman D.J., King G.C.P., Millar D.H.M., Robin G.D. (1979). Pressure-melting effect in basal ice of temperate glaciers: Laboratory studies and field observations under glacier Dargentiere. *Journal of Glaciology*, **23**, 259-271.

Hassanpouryouzband A., Yang J., Tohidi B., Chuvilin E., Istomin V., Bukhanov B., Cheremisin A. (2018). “CO_2 Capture by Injection of Flue Gas or CO_2-N_2 Mixtures into Hydrate Reservoirs: Dependence of CO_2 Capture Efficiency on Gas Hydrate Reservoir Conditions”. *Environmental Science and Technology*, **52**, 4324-433.

Head K.H. (1998). Manual of Soil Laboratory Testing, V3, 2nd, John Wiley & Sons, Chichester, England, 222-223, 19-20.

Holder G.D., Kamath V.A., Godbole S.P. (1984). The potential of natural gas hydrates as an energy resource. *Annual Review of Energy,* **9**, 427-445.

Hyodo M., Li., Yoneda J., Nakata Y., Yoshimoto N., Nishimura A., Song Y. (2013). Mechanical behaviour of gas-saturated methane hydrate-bearing sediments. *Journal of Geophysical Research*: Solid Earth, **118**, 5185-5194.

Istomin V., Chuvilin E., Bukhanov B., Uchida T. (2017). Pore water content in equilibrium with ice or gas hydrate in sediments. *Cold Regions Science and Technology.* **137**, 60–67.

Jones S.J. (1982). The confing compressive strength of polycrystalline ice. *Journal of Glaciology*, **28**, 171-177.

Judge A.S. and Majorowicz J.A. (1992). Geothermal conditions for gas hydrate stability in the Beaufort-Mackenzie area: the global change aspect. *Global and Planetary Change*, **98**, 251-263.

Konno Y., Yoneda J., Egawa K., Ito T., Jin Y., Kida M., Suzuki K., Fujii T., Nagao J. (2015). Permeability of sediment cores from methane hydrate deposit in the Eastern Nankai Trough. Marine and Petroleum Geology, **66**, 487-495.

Kurihara M., Sato A., Funatsu K., Ouchi H., Yamamoto K., Numasawa M., Ebinuma T., Narita H., Masuda Y., Dallimore S.R., Wright F., Ashford D. (2010). Analysis of production data for 2007-2008 Mallik gas hydrate production tests in Canada. SPE 132155, presented at *the CPS/SPE International Oil & Gas Conference and Exhibition* in China, Beijing, China, 8-10 June 2010.

Kvenvolden K.A. (1988). Methane hydrates—a major reservoir of carbon in the shallow geosphere? *Chemical Geology,* **71**, 41-51.

Lee J.Y., Francisca F.M., Santamarina J.C., Ruppel C. (2010). Parametric study of the physical properties of hydrate-bearing sand, silt, and clay sediments: 2. Small-strain mechanical properties. *Journal of Geophysical Research*, **115**, B11105.silt

Lee J.Y., Santamarina J.C., Ruppel C. (2008). Mechanical and electromagnetic properties of northern Gulf of Mexico sediments with and without THF hydrates. *Marine and Petroleum Geology*, **25**, 884-895.

Li Y., Liu W., Zhu Y., Chen Y., Song Y., Li Q. (2016). Mechanical behaviors of permafrost-associated methane hydrate-bearing sediments under different mining methods. *Applied Energy*, **162**, 1627–1632.

Liu W., Zhao J., Luo Y., Song Y., Li Y., Yang M., Zhang Y., Liu Y., Wang D. (2013). Experimental measurements of mechanical properties of carbon dioxide hydrate-bearing sediments. *Marine and Petroleum Geology*, **46**, 201-209.

Liu Z., Dai S., Ning F., Peng L., Wei H., Wei C. (2018). Strength estimation for hydrate-bearing sediments from direct shear tests of hydrate-bearing sand and silt. *Geophysical Research Letters*, **45**, 715–723.

Masuda Y., Maruta H., Naganawa S., Amikawa K. (2011). Methane recovery from hydrate-bearing sediments by N_2-CO_2 gas mixture injection: experimental investigation on CO_2-CH_4 exchange ratio. *Proceedings of the 7th International Conference on Gas Hydrates, Edinburgh, Scotland, United Kingdom, July 17-21, 2011*

Makogon Y.F., Trebin F.A., Trofimuk A.A., Tsarev V.P., Cherskiy N.V. (1972). Detection of a Pool of Natural Gas in a Solid (Hydrate Gas) State. *Doklady Academy of Sciences, USSR, Earth Science Section*, **196**, 197-200.

Masui A., Haneda H., Ogata Y., Aoki K. (2005). Effects of methane hydrate formation on shear strength of synthetic methane hydrate sediments. Proceedings of the 15th International Offshore and Polar Engineering Conference, Seoul, Korea, June 19-24, 2005.

Max M. D. and Johnson A. H. (2016). Exploration and Production of Oceanic Natural Gas Hydrate; Springer: New York.

Max M.D. and Lowrie A., (1996). Oceanic methane hydrates: A “frontier” gas resource. *Journal of Petroleum Geology*, **19**, 41-56.

Metz, B.; Davidson, O.; de Coninck, H. C.; Loos, M.; Meyer, L. A., Eds. (2005). *IPCC special report on carbon dioxide capture and storage*; Cambridge University Press: Cambridge, United Kingdom and New York, NY, USA.

Milkov A.V. (2004). Global estimates of hydrate-bound gas in marine sediments: how much is really out there? *Earth-Science Reviews,* **66**, 183-197.

Mitchell J.K. (1993). *Fundamentals of Soil Behaviour (Second Edition)*. John Wiley & Sons: New York, USA. 343, 344; 131-141.

Miyazaki K., Masui A., Sakamoto Y., Aoki K., Tenma N., Yamaguchi T. (2011). Triaxial compressive properties of artificial methane-hydrate-bearing sediment. *Journal of Geophysical Research*, **116**, B06102.

Nisbet E.G. and Piper D.J.W. (1998). Giant submarine landslide. *Nature*, **392**, 329–330.

Ohgaki K., Takano K., Sangawa H., Matsubara T., Nakano S. (1996). Methane exploitation by carbon dioxide from gas hydrates- Phase Equilibria for CO_2-CH_4 mixed hydrate system. *Journal of Chemical Engineering of Japan*, **29**, 478-483.

Parameswaran V.R., Paradisa M., Hanada Y.P. (1989). Strength of frozen sand containing tetrahydrofuran hydrate. *Cannadian Geotechnical Journal*, **26**, 479-483.

Paull C.K., Ussler W., Dillon W.P. (1991). Is the extent of glaciation limited by marine gas-hydrates? *Geophysical Research Letters*, **18**, 432–434. https://doi.org/10.1029/91GL00351.

Priest J.A., Best A.I., Clayton C.R.I. (2005). A laboratory investigation into the seismic velocities of methane gas hydrate-bearing sand. *Journal of Geophysical Research-Solid Earth*, **110** (B4), B04102.

Safronov A.F., Sgits E.Y., Grigor'ev M.N., Semenov M.E. (2010). Formation of gas hydrate deposits in the Siberian Arctic shelf. *Russian Geology and Geophysics*, **51**, 83-87.

Santamarina J.C., Dai S., Terzariol M., Jang J., Waite W.F., Winters W.J., Nagao J., Yoneda J., Konno Y., Fujii T., Suzuki K. (2015). Hydro-bio-geomechanical properties of hydratebearing sediments from Nankai Trough. *Marine and Petroleum Geology*, **66**, 434–450.

Schoderbek D., Martin K.L., Howard J., Silpngarmlet S., Hester K. (2012). North slope hydrate fieldtrial: CO_2/CH_4 exchange. OTC 23725, presented at *the Arctic Technology Conference*, Houston, Texas, U.S.A., 3-5 December 2012.

Seyfried M.S. and Murdock M.D. (1997). Use of air permeability to estimate infiltrability of frozen soil. *Journal of Hydrology*, **202**, 95–107.

Shakhova N., Semiletov I., Leifer I.,Salyuk A., Rekant P., Kosmach D. (2010). Geochemical and geophysical evidence of methane release over the East Siberian Arctic Shelf. Journal of Geophysical Research, **115**, C08007, doi:10.1029/2009JC005602.

Sloan E.D. and Koh C.A. (2007). *Clathrate Hydrates of Natural Gases*. CRC Press, Taylor & Francis Group: Boca Raton.

Song Y., Zhu Y., Liu W., Li Y., Lu Y., Shen Z. (2016). The effects of methane hydrate dissociation at different temperatures on the stability of porous sediments. *Journal of Petroleum Science and Engineering,* **147**, 77–86.

Tsytovich N.A. (1975). The mechanics of frozen ground, McGraw-Hill Book Company, New York, NY.

Vyalov S.S. (1965). Rheological properties and bearing capacity of frozen soils. U.S. Army, Corps of Engineers. Cold Regions Research and Engineering Laboratory in Hanover, New Hampshire, USA. Translation 74.

Waite W.F., Santamarina J.C., Cortes D.D., Dugan B., Espinoza D.N., Germaine J., Jang J., Jung J.W., Kneafsey T.J., Shin H., Soga K., Winters W.J., Yun T.-S. 2009. Physical properties of hydrate bearing sediments. *Reviews of Geophysics*, **47**, RG4003.

Waite W.F., Winter W.J., Mason D.H. (2004). Methane hydrate formation in partially water-saturated Ottawa sand. *American Mineralogist*, **89**, 1202-1207.

Westbrook G.K., Thatcher K.E., Rohling E.J., M. Piotrowski A.M., Pälike H., Osborne A.H., Nisbet E.G., Minshull T.A., Lanoisellé M., James R.H., Hühnerbach V., Green D., Fisher R.E., Crocker A.J., Chabert A., Bolton C., Beszczynska-Möller A., Berndt C., Aquilina A. (2009). Escape of methane gas from the seabed along the West Spitsbergen continental margin. *Geophysical Research Letters*, **36**, L15608, doi:10.1029/2009GL039191.

Winters, W.J., Pecher I.A., Booth J.S., Mason D.H., Relle M.K., Dillon W.P. (1999). Properties of samples containing natural gas hydrate from the JAPEX/JNOC/GSC Mallik 2L-38 gas hydrate research well, determined using Gas Hydrate And Sediment Test Laboratory Instrument (GHASTLI): *Geological Survey of Canada Bulletin*, Part **544**: 241-250.

Yakushev V.S. and Chuvilin E.M. (2000). Natural gas and gas hydrate accumulations within permafrost in Russia. *Cold Regions Science and Technology*, **31**, 189–197.

Yang J., Okwananke A., Tohidi B., Chuvilin E., Maerle K., Istomin V., Bukhanov B., Cheremisin A. (2017). Flue gas injection into gas hydrate reservoirs for methane recovery and carbon dioxide sequestratio. *Energy Conversion and Management*, **136,** 431–438.

Yang L., Falenty A., Chaouachi M., Haberthür D., Kuhs W.F. (2016). Synchrotron X-ray computed microtomography study on gas hydrate decomposition in a sedimentary matrix. *Geochemistry, Geophysics, Geosystems*, **17**, 3717-3732.

Yershov E.D. (1998). General Geocryology. Cambridge: Cambridge University Press. 580.

Yoneda J., Masui A., Konno Y., Jin Y., Egawa K., Kida M., Ito T., Nagao J., Tenma N. (2015). Mechanical properties of hydrate-bearing turbidite reservoir in the first gas production test site of the Eastern Nankai Trough. *Marine and Petroleum Geology*, **66**, 471-486.

Yun T.S., Santamarina, Ruppel C. (2007). Mechanical properties of sound, silt, and clay containing tetrahydrofuran hydrate. *Journal of Geophysical Research,* **112**, B04106.

Zhang S., Lai Y., Sun Z., Gao Z. (2007). Volumetric strain and strength behaviour of frozen soils under confinement. *Cold Regions Science and Technology*, **47**, 263–270.

Zhao J., Yang L., Xue K., Lam W., Li Y., Song Y. (2014). In situ observation of gas hydrates growth hosted in porous media. *Chemical Physics Letters*, **612**, 124-128.